Visible and NIR Upconverting Er^{3+}–Yb^{3+} Luminescent Nanorattles and Other Hybrid PMO-Inorganic Structures for In Vivo Nanothermometry

Anna M. Kaczmarek,* Markus Suta, Hannes Rijckaert, Anatolii Abalymov, Isabel Van Driessche, Andre G. Skirtach, Andries Meijerink,* and Pascal Van Der Voort

Lanthanide-doped luminescent nanoparticles are an appealing system for nanothermometry with biomedical applications due to their sensitivity, reliability, and minimal invasive thermal sensing properties. Here, four unique hybrid organic–inorganic materials prepared by combining β-NaGdF$_4$ and PMOs (periodic mesoporous organosilica) or mSiO$_2$ (mesoporous silica) are proposed. PMO/mSiO$_2$ materials are excellent candidates for biological/biomedical applications as they show high biocompatibility with the human body. On the other hand, the β-NaGdF$_4$ matrix is an excellent host for doping lanthanide ions, even at very low concentrations with yet very efficient luminescence properties. A new type of Er^{3+}–Yb^{3+} upconversion luminescence nanothermometers operating both in the visible and near infrared regime is proposed. Both spectral ranges permit promising thermometry performance even in aqueous environment. It is additionally confirmed that these hybrid materials are non-toxic to cells, which makes them very promising candidates for real biomedical thermometry applications. In several of these materials, the presence of additional voids leaves space for future theranostic or combined thermometry and drug delivery applications in the hybrid nanostructures.

1. Introduction

Temperature measurements in biomedicine are of great importance, as temperature plays an essential role in biological systems.[1] Conditions involving inflammation and diseases such as cancer are accompanied by hyperlocal temperature changes in the affected tissues. Therefore, precise temperature measurements in the physiological range (20–50 °C) are crucial.[2] Up to date, temperature sensing is possible by robust and already commercially available techniques, such as thermocouples or infrared imaging.[3] However, optical measurements at the nanoscale have the advantage of being remote and non-invasive and thus, make it possible to significantly improve the spatial resolution and reveal phenomena that are otherwise inaccessible to any alternative conventional thermometers. Examples include local and precise measurements of the temperature in cells and even the organelles within them.[1]

Among the various possibilities of temperature detection by means of luminescence, the by far most widely employed type is based on the detection of a luminescence intensity ratio between two emission bands originating either from two thermally coupled emissive states of a single ion or from two different ions interacting by a thermally assisted energy transfer.[4]

Lanthanide-doped luminescent nanoparticles are an appealing nanothermometry system for biomedical applications due to their high thermal sensitivity, reliability, and minimally invasive thermal sensing properties.[5,6] Lanthanides have shown to be particularly well suited for luminescence thermometry due to their high number of closely lying emissive excited states originating from the 4f^n configuration that allow for luminescence detection from the ultraviolet (UV) over the visible to near infrared (NIR) range.[7–20] The well-shielded nature of the 4f orbitals and the resulting 4f^n → 4f^n-based narrow emission peaks accompanied by their relatively low sensitivity to variations in the chemical environment do not only minimize spectral overlap between the closely lying radiative transitions stemming from the thermally coupled excited states. They are also perfectly suited conditions for a precise determination of spectral intensity ratios for various applications.[21,22]

The development of efficiently emitting nanothermometers for the sake of in vivo applications is very challenging. The luminescent ions embedded in the nanothermometers have to

Prof. A. M. Kaczmarek, Dr. H. Rijckaert, Prof. I. Van Driessche,
Prof. P. Van Der Voort
Department of Chemistry
Ghent University
Krijgslaan 281-S3, Ghent 9000, Belgium
E-mail: anna.kaczmarek@ugent.be
Dr. M. Suta, Prof. A. Meijerink
Debye Institute for Nanomaterials Science
Utrecht University
Princetonplein 1, Utrecht 3584 CC, The Netherlands
E-mail: a.meijerink@uu.nl
A. Abalymov, Prof. A. G. Skirtach
Department of Biotechnology
Faculty of Bioscience Engineering
Ghent University
Ghent 9000, Belgium

The ORCID identification number(s) for the author(s) of this article can be found under https://doi.org/10.1002/adfm.202003101.

**ADVANCED
SCIENCE NEWS**
www.advancedsciencenews.com

**ADVANCED
FUNCTIONAL
MATERIALS**
www.afm-journal.de

be efficiently excitable in the NIR region of the electromagnetic spectrum and preferably also emit in the deeper NIR range, for which tissue is almost transparent. On top, they have to be completely non-toxic to human tissue and biocompatible with the human body. Any advance the development in such new nanothermometric materials doubtlessly also leaves space for a movement towards theranostic applications.

Although lanthanide-doped luminescent nanoparticles have already met several of the previously mentioned requirements, some issues still remain such as biocompatibility, water dispersability, or possible routes to combine diagnostics with treatment (for example photodynamic therapy, PDT). A common way to overcome at least the first two concerns is coating of the inorganic nanoparticles with a silica shell.[23,24]

In this work, we present four new hybrid materials developed by combining inorganic materials with periodic mesoporous organosilica (PMOs) or mesoporous silica (mSiO$_2$).[25,26] PMOs are especially interesting, as they show excellent biocompatibility with the human body and even supersede silica itself in that regard.[25] In several of these materials, the presence of additional voids would allow theranostic applications, for example additional loading of the hybrid nanostructures with drugs for additional drug delivery.

Desirably, the spectral range of both the absorption and luminescence of the nanothermometers aiming at biological applications should be restricted to the three so-called biological windows (BWs), in which both tissue absorption and scattering are minimized (BW-I: 650–950 nm, BW-II: 1000–1350 nm, and BW-III: 1500–1800 nm).[27] BW-I has the inconvenience of signal interference by tissue autofluorescence (background fluorescence originating from biomolecules), yet its remarkable tissue penetration properties are often exploited for effective NIR laser excitation. As mentioned, the desirable situation

for bioimaging techniques is excitation in BW-I. Here, tissue already shows sufficiently low absorption/scattering. However, emission should be spectrally much more separated to allow for sufficient contrast. Therefore, most applicational systems should absorb in BW-I, but emit in BW-II and BW-III. We have shown that for all presented materials upon excitation close to BW-I at 980 nm (BW-I ends at 950 nm), reliable thermometric performance between 20 and 60 °C can be proven by the upconverted green emission of Er^{3+} in the visible range even in water. Usage of the same excitation wavelength (980 nm) also allowed detection of emission from the thermally coupled $^2H_{11/2}$ and $^4S_{3/2}$ levels into the higher lying $^4I_{13/2}$ ground level located in the red-NIR and NIR region (BW-I) even in water in one of those materials. Additionally, all materials were shown to be completely non-toxic to human fibroblastic cells even at high concentrations proving their excellent potential as future nanothermometers for biological systems.[28]

2. Results and Discussion

An overview of the developed PMO/mSiO$_2$-inorganic hybrid materials is given in **Scheme 1**. The detailed synthesis routes of the materials are presented in the Experimental Section. In materials **1** and **2** (nanorattles), voids are created by etching out SiO$_2$ for the potential purpose of future loading with drugs for drug delivery or a PDT agent for potential theranostics at the next stage (detection and therapy at the same time). The four materials were characterized by powder XRD before and after loading with β-NaGdF$_4$:Er^{3+}, Yb^{3+}, and transmission electron microscopy (TEM), scanning TEM with high-angle annular dark-field detector (HAADF-STEM), and energy dispersive X-ray (EDX) mapping to confirm that the targeted materials with
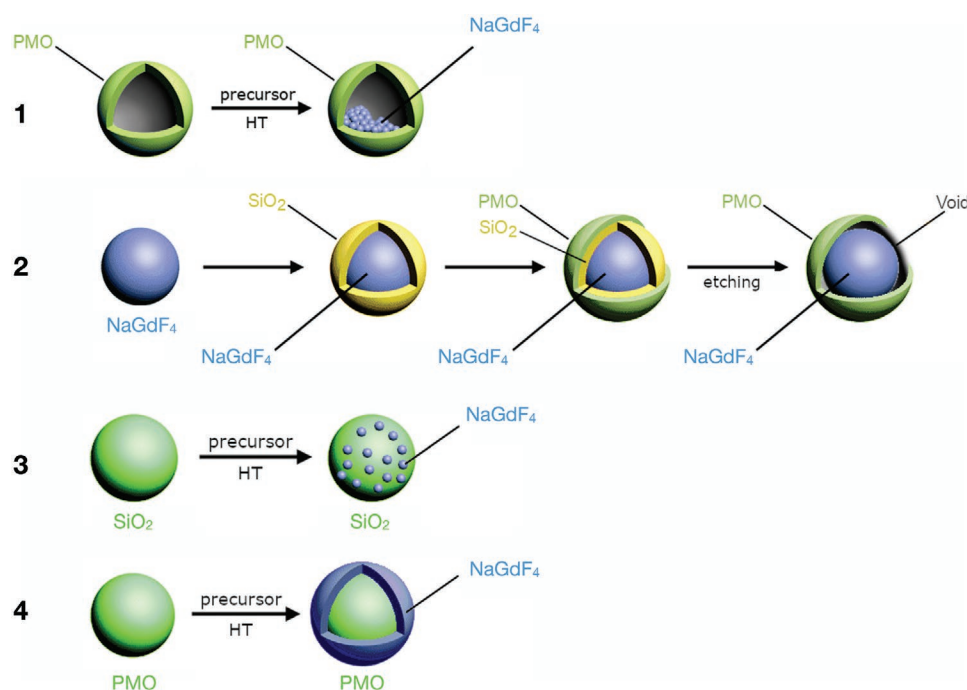
Scheme 1. Schematic illustration for the preparation of the four hybrid PMO/mSiO$_2$-inorganic materials.
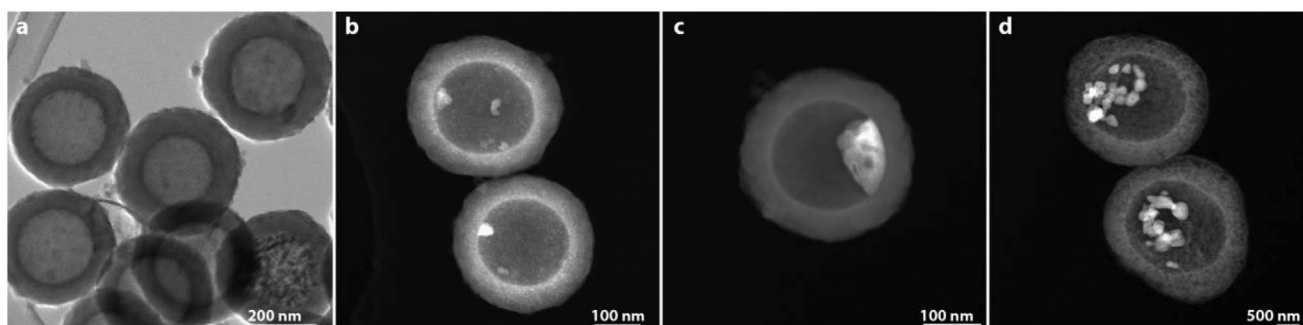
Figure 1. TEM and HAADF-TEM images of a) hollow BTEB PMO particles (scale bar 200 nm), b–d) hollow BTEB PMO particles loaded with varying amounts of β-NaGdF$_4$:Er^{3+}, Yb^{3+} (compound **1**) (scale bar 200 nm or 2 µm). The amount of loading was varied by changing the precursor concentration and reaction time.

desirable morphology were obtained. The powder XRD patterns for all samples and their precursors (e.g., mesoporous silica before doping with nanoparticles) are depicted in Figures S1,S2, Supporting Information. In **Figure 1**, the (S)TEM images for compound **1** are presented. Compound **1** was obtained by first growing a SiO$_2$ core and then a BTEB PMO (BTEB—1,4-Bis(triethoxysilyl)benzene) shell around it. A scheme overviewing the general synthesis of PMO-type materials has been presented in Scheme S1, Supporting Information. The SiO$_2$ was etched in a later step using Na$_2$CO$_3$ leaving a hollow PMO sphere. Next, under vacuum the hollow BTEB sphere was loaded with Ln(CF$_3$COO)$_3$ precursors and heat treated at 300 °C. Figure 1a shows the BTEB hollow spheres. Figure 1b–d visualize the nanorattles after loading with different amounts of β-NaGdF$_4$ (by control of the precursor concentration and reaction time). The presence of β-NaGdF$_4$:Er^{3+}, Yb^{3+} inside the hollow PMOs was confirmed by EDX mapping (Figure S3, Supporting Information). TEM images of **2** are depicted in **Figure 2**. Figure 2a shows the 5 nm β-NaGdF$_4$:Er^{3+},Yb^{3+} nanoparticles obtained in a co-precipitation synthesis that were used further on in the synthesis of compound **2**. They were first coated with a shell of SiO$_2$ and next with a PMO shell (PMO shell was formed from a mixture of APTES—(3-aminopropyl)triethoxysilane and BTEB) (Figure 2b,c). In order to create voids and additionally enhance the luminescence properties, SiO$_2$ was etched

out using PVP (poly(vinylpyrrolidinone)) solution in the last step (Figure 2d). Compounds **3** and **4** were prepared in the same synthesis batch. For compound **3**, mesoporous SiO$_2$ (mSiO$_2$) particles of around 50 nm in size were prepared (**Figure 3**a). For compound **4**, the DPA PMO nanoparticles prepared from 5% *N,N*-bis(trimethoxysilylpropyl)-2,6-pyridine dicarboxamide and 95% tetraethyl orthosilicate were employed.[29] The particles were round but a bit elongated and around 50–70 nm in size (Figure 3b). The powder XRD patterns of mSiO$_2$ particles are shown in Figure S1b, Supporting Information, and the characteristic broadened Bragg reflection due to the amorphous nature of the silica particles is observed.[30] In Figure S1c, Supporting Information, the XRD pattern of compound **4** shows a strong reflection due to the (100) plane at low angle 2θ as well as two short second-order reflections due to the (110) and (200) planes are detected. This is typical for materials with a hexagonal arrangement of uniform pores and confirms that it is a PMO-type material.[31] To obtain compounds **3** and **4**, the mSiO$_2$ and DPA PMO particles were soaked in lanthanide (containing Gd, Er, Yb) and sodium trifluoroacetic acid precursors dissolved in a small amount of water and left overnight at 40 °C with stirring. Afterward, the particles were centrifuged at low RPMs (2000 RPM), dried, and heat treated at corresponding temperatures (300 °C for DPA PMO and 500 °C for mSiO$_2$), which yielded the final products. In order to evaluate the porosity of
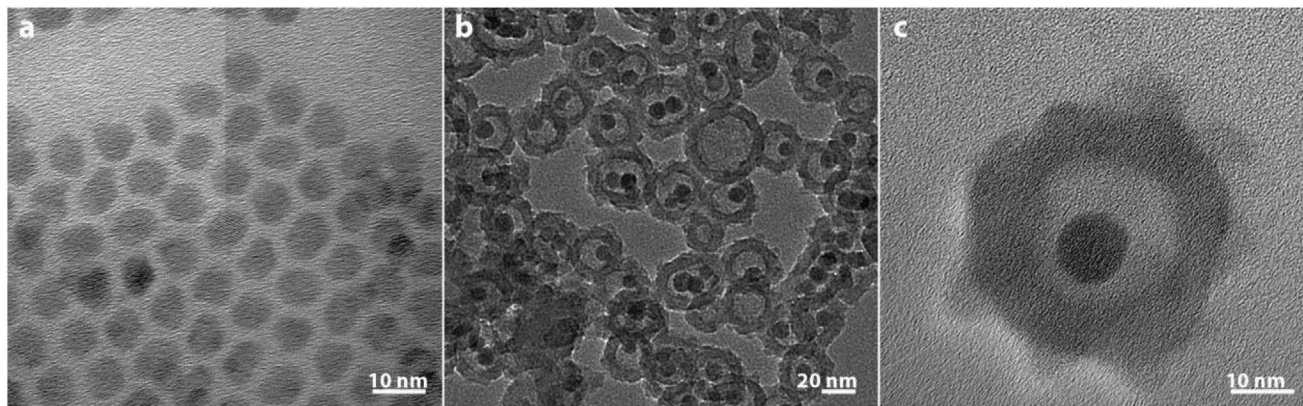

Figure 2. TEM images of a) 5 nm β-NaGdF$_4$:Er^{3+}, Yb^{3+} nanoparticles (scale bar 5 nm), b) PMO@SiO$_2$@β-NaGdF$_4$:Er^{3+}, Yb^{3+} (before etching; scale bar is 20 nm), and c) PMO@_@β-NaGdF$_4$:Er^{3+}, Yb^{3+} after etching (compound **2**; scale bar is 50 nm).

ADVANCED
SCIENCE NEWS
www.advancedsciencenews.com

ADVANCED
FUNCTIONAL
MATERIALS
www.afm-journal.de

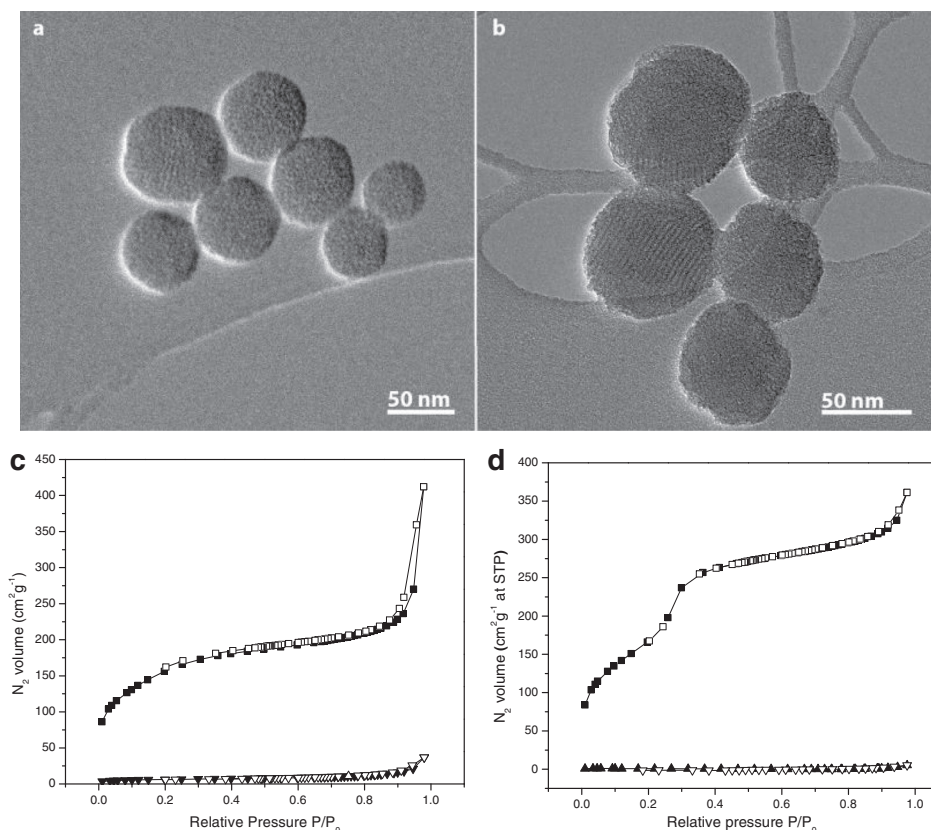**Figure 3.** TEM images of a) mSiO$_2$ nanoparticles and b) DPA-PMO nanoparticles (scale bar is 50 nm). N$_2$ sorption-desorption isotherms: c) mSiO$_2$ nanoparticles and compound **3**, d) DPA-PMO nanoparticles and compound **4** (the pristine materials show the higher isotherms and compound **3** and **4** show the lower isotherms).

the obtained hybrid materials, N$_2$ sorption measurements were performed. A drastic drop of the BET surface area in the hybrid materials compared to mSiO$_2$ (from 572 to 22 m^2 g^{-1}) and DPA PMO (from 895 to 3 m^2 g^{-1}) was observed, which suggests an almost complete blockage of the pores. EDX mapping showed that in compound **3** the Na, F, and lanthanide elements are only distributed in certain areas of the mSiO$_2$ material. This observation suggests that most likely small β-NaGdF$_4$ nanoparticles crystallize inside the pores of the mSiO$_2$ (Figure S4, Supporting Information). From the characterization of compound **3** it is not completely clear how the β-NaGdF$_4$ builds into the mSiO$_2$ support. N$_2$ sorption and EDX mapping suggest that the β-NaGdF$_4$ is located in some areas of the mSiO$_2$ almost completely clogging up the pores. However, the powder XRD pattern shows some sharp peaks along with other broader ones. This may suggest that β-NaGdF$_4$ builds inside the pores as elongated structures, which have different dimensions. To support our theory that nano-sized particles are formed we have measured the upconversion luminescence of **3** at 10 K to verify if the emission peaks show clearly resolved splitting patterns at low temperature that indicate a high degree of crystallinity. No such splitting was observed even at 10 K (Figure S5, Supporting Information). The ratio of the green to red emission (the $^2H_{11/2} \rightarrow {}^4I_{15/2}$ and $^4S_{3/2} \rightarrow {}^4I_{15/2}$ transitions compared to the $^4F_{9/2} \rightarrow {}^4I_{15/2}$) also suggests a nanoscale size of the particles.[32] The powder XRD patterns of the compounds (Figure S2,

Supporting Information) reveal both sharp and some broad Bragg reflections within one compound, respectively, and thus indicate that most likely rod-like anisotropic crystallites grow within the pores that give rise to such a texture effect. On the other hand, for compound **4**, it can be seen from the TEM-EDX that a layer of the Na, Gd, F, Yb, and Er elements covers the PMO particles, forming a shell of β-NaGdF$_4$:Er^{3+}, Yb^{3+} around the DPA PMO, which explains the complete loss of porosity (Figure S6, Supporting Information).

The manufactured compounds were tested for their luminescence properties upon excitation with a 980 nm continuous wave (CW) laser both in solid state and aqueous suspension. The temperature-dependent emission spectra (30–60 °C) of the powdered compounds are presented in Figure S8, Supporting Information. Green upconversion emission due to the $^2H_{11/2} \rightarrow {}^4I_{15/2}$ and $^4S_{3/2} \rightarrow {}^4I_{15/2}$ transitions of Er^{3+} was observed.[33,34] As expected, the intensity of the $^2H_{11/2} \rightarrow {}^4I_{15/2}$-based emission increases with increasing temperature due to enhanced thermal population of the $^2H_{11/2}$ level by the $^4S_{3/2}$ level. However, for final in vivo applications, the performance of the system in an aqueous suspension has to be critically verified. All four hybrid materials showed reliable thermometric performance in water in the range between 20 and 60 °C upon excitation at 980 nm (close to BW-I) and acquisition of the upconversion luminescence spectrum in the green range. For the sake of demonstration, only the respective thermometric properties of compound
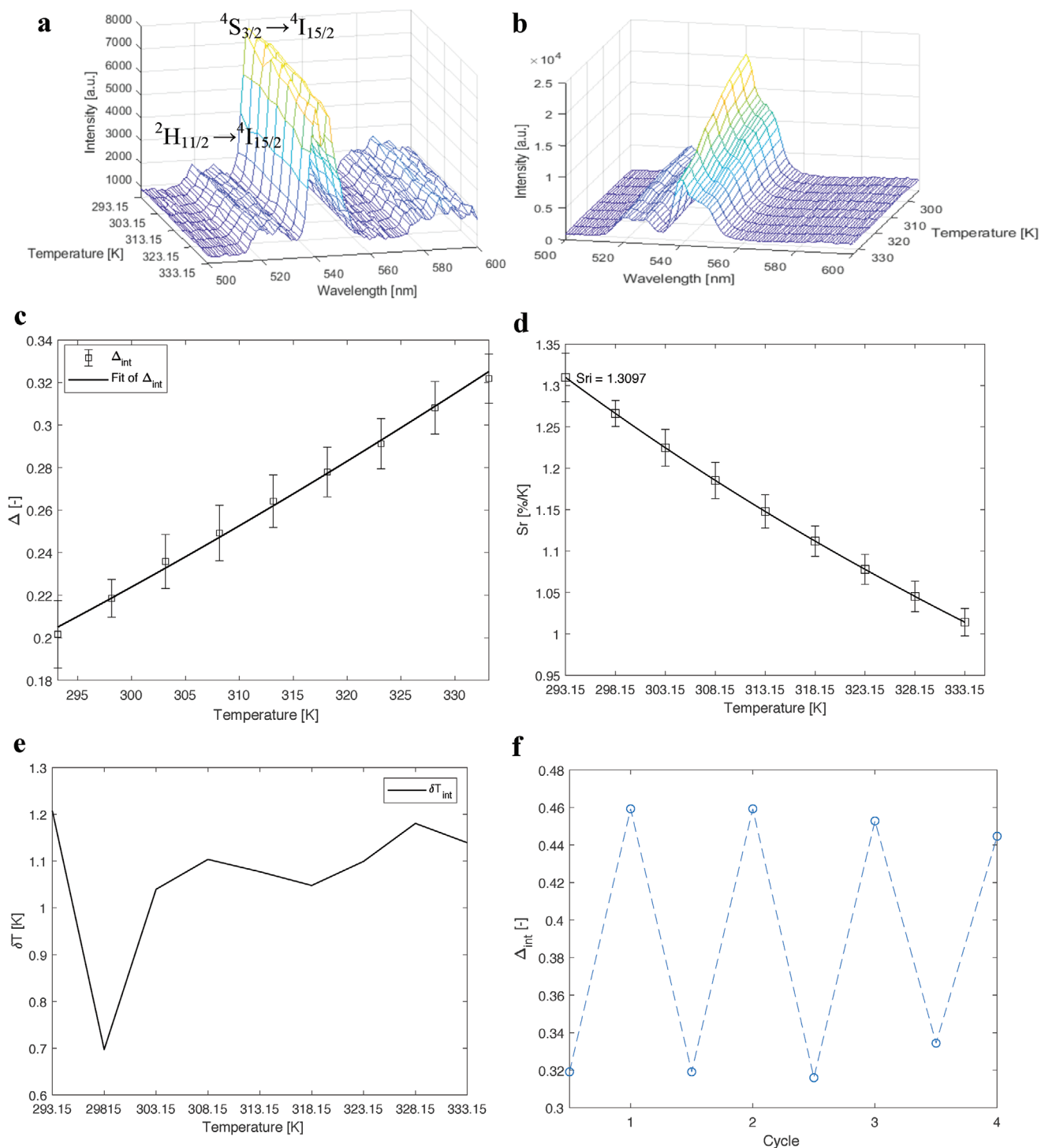
Figure 4. a) Emission map of **2** before etching recorded in H_2O at 293.15–333.15 K (20–60 °C), b) emission map of **2** after etching recorded in H_2O at 293.15–333.15 K (20–60 °C), c) plot showing the calibration curve for **2** after etching upon usage of Equation (1). The points show the experimental delta parameters (see Equation (1)) and the solid line shows the least-squares fit of the experimental points ($R^2 = 0.9967$). d) Plot of the relative sensitivity (S_r) at varying temperatures (293.15–333.15 K) for **2** after etching, the solid line is a guide for the eyes. e) Graph depicting the temperature uncertainty for **2** after etching over the regarded temperature range. f) Graph presenting the cycle tests for compound **2** after etching (97–98% repeatability).

2 are discussed in this manuscript (**Figure 4**). The analogous thermometric data upon usage of the visible upconversion luminescence of Er^{3+} for the remaining compounds (**1**, **3**, and **4**) are presented in detail in Figures S8–S10, Supporting Information. All materials show very promising thermometric performance in water in the physiological temperature regime. We compared

**ADVANCED
SCIENCE NEWS**

www.advancedsciencenews.com

**ADVANCED
FUNCTIONAL
MATERIALS**

www.afm-journal.de

the luminescence properties at varying temperatures (measured in water) of **2** before and after etching of the SiO_2 shell (Figure 4a,b). An enhancement in the luminescence intensity is visible after etching, which is explained by the fact that no silica is in immediate contact with the Er^{3+} ions on the surface of the β-NaGdF$_4$ particles that could otherwise induce additional non-radiative quenching processes by means of the higher vibrational energies of present −OSi and especially Si−OH surface groups.[35] Only the etched material was thus further investigated. The change in intensity of the two observed emission peaks (519 and 540 nm) with temperature change is plotted in Figure S11, Supporting Information. In order to evaluate whether the material performs well as a thermometer the integrated areas under the 519 and 540 nm peaks were used to calculate the $\Delta = I_{519}/I_{540}$ ratio (Figure 4c). The data points could be well fitted with Boltzmann's law (see Equation [1]):

$$\Delta = \alpha \exp\left(-\frac{\Delta E}{k_B T}\right) \tag{1}$$

where $\alpha = C\, g_2/g_1$. C contains information about the ratio of the radiative transition probabilities from the two thermally coupled levels to the addressed ground level, while g_2 and g_1 are the $(2J + 1)$-fold degeneracies of the $^2H_{11/2}$ and the $^4S_{3/2}$ level, respectively, ΔE is the effective energy gap between the two excited levels.[36,37] A least-squares fit to the temperature-dependent values of Δ yielded $\Delta E = (782 \pm 25)$ cm^{-1} ($R^2 = 0.9967$), which is in very good agreement with the spectroscopically expected value of the energy difference between the $^2H_{11/2}$ and $^4S_{3/2}$ level.[38] The plot showing the thermometric calibration curve for **2** is presented in Figure 4d. The maximum relative sensitivity, Sr, was calculated using Equation (2) and is equal to 1.31% K^{-1} at 293.15 K.

$$S_r = 100\% \times \left|\frac{1}{\Delta}\frac{\partial \Delta}{\partial T}\right| = 100\% \times \frac{\Delta E}{k_B T^2} \tag{2}$$

Temperature uncertainty, which can be calculated employing Equation (3), is the most important parameter to assess the reliability of a thermometer. A low temperature uncertainty was observed for **2** with $\delta T < 1.2$ K throughout the whole studied temperature range (Figure 4e).

$$\delta T = \frac{1}{S_r}\frac{\delta \Delta}{\Delta} \tag{3}$$

Last, in order to evaluate whether the material could be used as a reliable thermometer more than once, cycle tests were performed and the repeatability was calculated using Equation (4):

$$R = 1 - \frac{\max|\Delta_c - \Delta_i|}{\Delta_c} \tag{4}$$

where Δ_c is the mean thermometric parameter and Δ_i is the value of each measurement of thermometric parameter.[20] The material showed 97–98% repeatability.

These results showed that all four hybrid inorganic-PMO materials are useful as well performing nanothermometers upon excitation of Yb^{3+} at 980 nm and detection of the upconverted green emission of Er^{3+}. Although many suggested systems for biological thermometry use that visible emission from the two thermally coupled $^2H_{11/2}$ and $^4S_{3/2}$ levels, the low tissue transparency in that regime does limit its applicability in biological systems.

Thus, we addressed the potential use of the Er–Yb upconversion couple in biological systems by investigation of the emission in the NIR range. Typically, only the green emission from the excited $^2H_{11/2}$ and $^4S_{3/2}$ levels to the lowest $^4I_{15/2}$ ground level is considered based on the interest on two-photon NIR-to-green upconversion. Once the two excited $^2H_{11/2}$ and $^4S_{3/2}$ levels of Er^{3+} are populated by energy transfer upconversion, however, also radiative transitions to the higher lying ground level $^4I_{13/2}$ should be possible, although this emission is weaker than the dominant emission to the $^4I_{15/2}$ ground state and thus more challenging to observe and measure accurately. Most of the studied systems (**1**, **2**, **3**) did not show appreciably intense NIR emission if dispersed in water. This is explained by the fact that the intensity of the desirable NIR luminescence based on the $^2H_{11/2}$, $^4S_{3/2} \rightarrow {}^4I_{13/2}$ transitions between 790 and 850 nm is critically dependent on the competitive multiphonon relaxation to the red emitting $^4F_{9/2}$ level of Er^{3+}. If the latter relaxation pathway is faster, the desirable NIR luminescence from the thermally coupled $^2H_{11/2}$ and $^4S_{3/2}$ levels is considerably quenched and leads to larger temperature uncertainties. Additional evidence for that interpretation could be obtained by a representative upconversion luminescence spectrum of compound **3** acquired at 10 K (see Figure S5, Supporting Information). The spectrum clearly reveals a dominant red emission related to the $^4F_{9/2} \rightarrow {}^4I_{15/2}$ transition at 660 nm even at that low temperature and leads to substantial losses in the excited state population of the $^2H_{11/2}$ and $^4S_{3/2}$ level. A schematic representation of the energy levels of the Yb^{3+} and Er^{3+} dopant ions and upconversion mechanism is given in **Scheme 2**.

However, the red $^4F_{9/2} \rightarrow {}^4I_{15/2}$-related emission in compound **4** is considerably lower in intensity. Concomitantly, compound **4** did not only show intense green upconverted luminescence due to the $^2H_{11/2}$, $^4S_{3/2} \rightarrow {}^4I_{15/2}$ transitions, but also appreciable emission in the NIR range. Upon laser excitation at 980 nm, the radiative $^2H_{11/2} \rightarrow {}^4I_{13/2}$ and $^4S_{3/2} \rightarrow {}^4I_{13/2}$
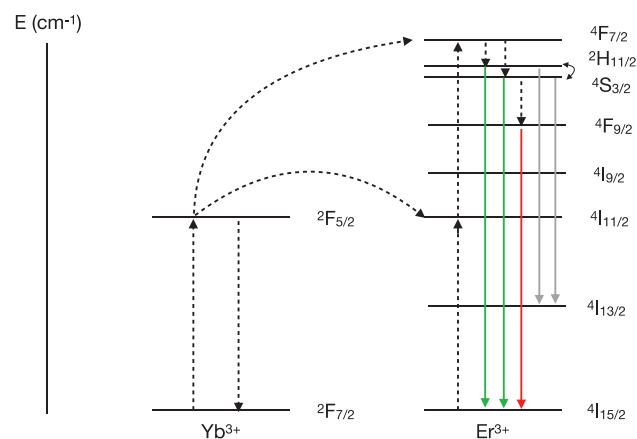
Scheme 2. Scheme showing energy levels of the Yb^{3+} and Er^{3+} dopant ions and upconversion mechanism. The temperature sensitivity is the result of the closely spaced $^2H_{11/2}$ and $^4S_{3/2}$ energy states.

**ADVANCED
SCIENCE NEWS**
www.advancedsciencenews.com

**ADVANCED
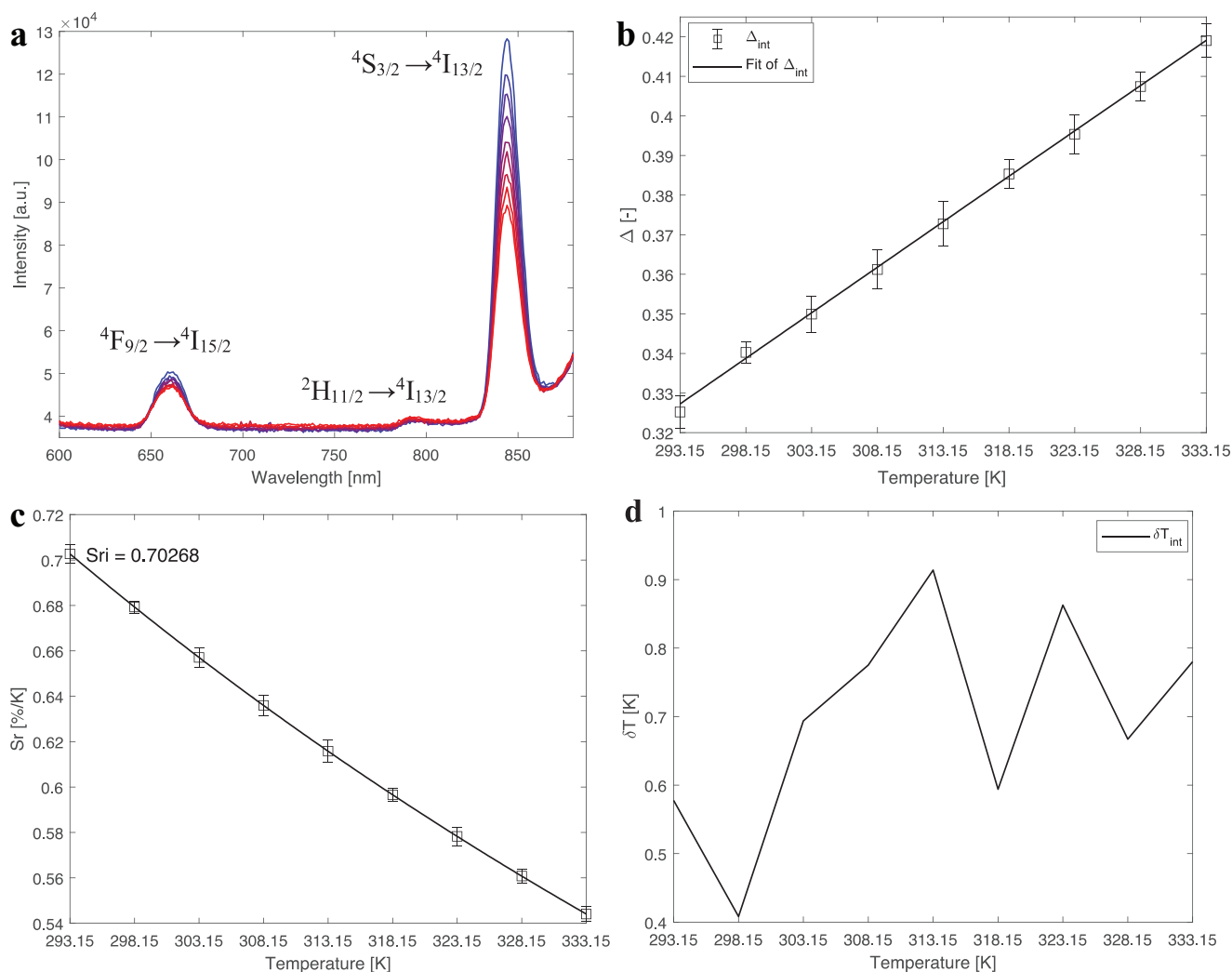FUNCTIONAL
MATERIALS**
www.afm-journal.de

Figure 5. a) Emission map of **4** recorded in H_2O at 293.15–333.15 K (20–60 °C) in the NIR range (BW-I) of the electromagnetic spectrum (blue color indicates lowest temperature, red color highest temperature), b) plot showing the calibration curve for **4** upon usage of Equation (1). The points show the experimental delta parameters (see Equation (1)) and the solid line shows the least-squares fit of the experimental points ($R^2 = 0.9964$). c) Plot of the relative sensitivity S_r at varying temperatures (293.15–333.15 K) for **4**, the solid line is a guide for the eyes. d) Graph depicting the temperature uncertainty for **4** over the regarded temperature range.

transitions are indeed observable with maxima at 790 and 840 nm, respectively.[38] The 790/840 nm ratio can thus be alternatively used for thermometry purposes matching the requirements for in vivo applications better. In **Figure 5**a, the emission map of **4** recorded at 293.15–333.15 K (20–60 °C) in water is presented. While the intensity of the $^4S_{3/2} \rightarrow$ $^4I_{13/2}$-related emission with increasing temperature shows a decrease, the $^2H_{11/2} \rightarrow$ $^4I_{13/2}$-related emission slightly increases with increasing temperatures as expected. The ratio of the respective integrated intensities, I_{790}/I_{840}, could be well fitted ($R^2 = 0.9964$) employing Equation (1). The fit gives an effective energy gap of $\Delta E = (636 \pm 21)$ cm^{-1}, which is slightly smaller than the spectroscopically expected value of the energy difference between the $^2H_{11/2}$ and $^4S_{3/2}$ excited levels (between 750 and 800 cm^{-1}).[38] The small deviation can originate from some weak $^4I_{9/2} \rightarrow$ $^4I_{13/2}$ emission around 790 nm which overlaps with the $^2H_{11/2} \rightarrow$ $^4I_{13/2}$ emission. The population of the $^4I_{9/2}$ level is

also temperature-dependent as it is partly induced by resonant cross-relaxation from $^2H_{11/2}$: [Er1, Er2]: [$^2H_{11/2}$, $^4I_{15/2}$] → [$^4I_{13/2}$, $^4I_{9/2}$]. The calibration curve for the thermometric performance using the two described emission peaks of **4** in the NIR range is depicted in Figure 5c. The maximum relative sensitivity, S_r, was calculated using Equation (2) and equals 0.70% K^{-1} at 293.15 K. A very low temperature uncertainty of $\delta T < 1$ K could be obtained for this thermometric probe throughout the whole studied temperature range (Figure 5d). Cycle tests revealed a repeatability of 95–99% (Figure S12, Supporting Information). This gives strong evidence that luminescence thermometry with the Er^{3+}–Yb^{3+} upconversion couple is not only possible with the conventional green upconverted emission by Er^{3+}, but can also be performed using the same thermally coupled $^4H_{11/2}$ and $^4S_{3/2}$ levels emitting in the BW-I, which has not been explored until recently.[39] The only requirement is a minimization of the multiphonon relaxation to the $^4F_{9/2}$ level, which
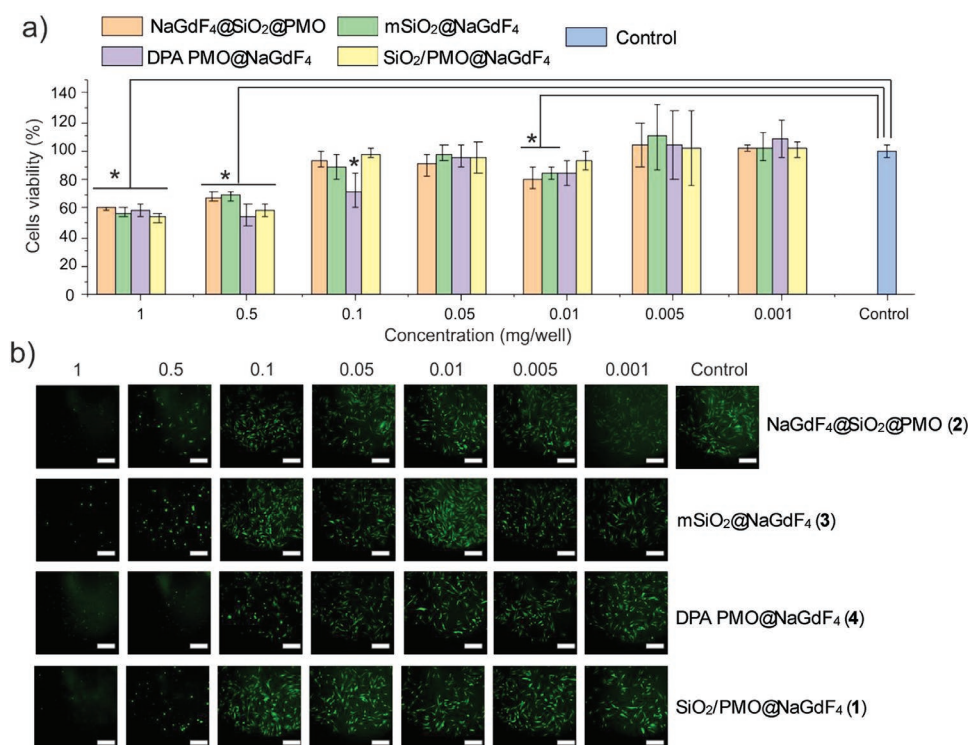
**ADVANCED
SCIENCE NEWS**
www.advancedsciencenews.com

**ADVANCED
FUNCTIONAL
MATERIALS**
www.afm-journal.de

Figure 6. Graph illustrating the cell viability (%) after exposure to different concentrations (0.001, 0.005, 0.01, 0.05, 0.1, 0.5, 1 mg per well) of compounds **1–4**. b) Fluorescence microscopy images of the cells at different compound concentrations (cells are green). The scale bar is 250 μm. Asterisks (*) indicate statistically significant differences from the control cell group. The statistical analysis was performed by ANOVA followed by the Tukey test ($p < 0.05$).

would otherwise lead to large intensity losses of the desirable NIR emission.

In order to fully assess the use of the proposed materials in biomedical systems, cytotoxicity tests on living cells were additionally conducted. Temperature plays an important role in living cells, for example, in studying intracellular process.[40] For these experiments, we used normal human dermal fibroblastic cells (NHDF cells). The viability tests indicated that compounds **1–4** are non-toxic (**Figure 6**). Particle toxicity towards fibroblastic cells occurred only at concentrations of 1 and 0.5 mg per well, which are very high concentrations of the compounds. Cell survival at those concentrations ranged from 50% to 60% (Figure 6a). Round cell morphology at 1 mg per well concentration indicates the inability to attach to the culture plastic (Figure 6b). At a 0.5 mg per well concentration, the cells do attach, but they do not have a spindle-shaped morphology, which is inherent to NHDF cells. ANOVA analysis also showed a strong difference between the control concentration as well as the 1 and 0.5 mg per well concentrations. This can be due to the mechanical pressure of the particles on the cells. Smaller concentrations of particles affect the cells to a much lower extent. The cell viability is 70% or higher (Figure 6a), which is considered as almost non-toxic.[41] There is also a statistically significant difference from the control for compound **4** with a 0.1 mg per well concentration, and for the **2** and **3** with a 0.01 mg per well concentration. Most likely this is due to the conglomeration of the nanoparticles.

For applications of luminescence nanothermometers in tissue or biological media, wavelength-dependent light absorption and scattering can affect the emission read-outs and result in deviations in temperature. A way to overcome this problem is calibration of the thermometer with tissue (e.g., by placing a small piece of the appropriate tissue in front of the measurement cuvette). This has been explored before, and showed promising results.[42] Additionally, in media with unknown scattering behavior, measurements at a known reference temperature (e.g., room temperature) provides a correction factor to mitigate this problem.[43] Another issue is the usage of a 980 nm laser excitation source. 980 nm CW lasers are well-established and cheaply available laser sources. However, the wavelength is in between BWs I and II as it is resonant with a vibrational overtone of water and can cause heating effects in aqueous media, including biological tissue. This is a general problem in the field. To overcome this issue the excitation can be shifted to a shorter wavelength, for example, 940 nm, which still falls within the range of the Yb^{3+} absorption band but is located in BW I.[44] A second solution is to further improve the upconversion efficiency and detection to allow accurate measurements with lower excitation power. It should be noted that careful control experiments at different laser powers should always be done to verify the absence of laser heating.

3. Conclusions

In this work, we explored four new hybrid materials developed by combining inorganic materials (β-NaGdF$_4$:Er^{3+}, Yb^{3+}) with PMOs or mSiO$_2$. PMOs are rapidly gaining attention due to

their excellent biocompatibility with the human body. In several of these materials the presence of additional voids allows future multifunctional applications such as theranostics that could be achieved by loading the hybrid nanoparticles with, for example, drugs for drug delivery. We could show that upon excitation in the NIR range at 980 nm, all four presented materials show strong green upconversion emission due to the Er^{3+} ions even if the materials are suspended in water. The respective $^2H_{11/2}$, $^4S_{3/2} \rightarrow {}^4I_{15/2}$ transitions allow for physiological thermometry between 20 and 60 °C with high luminescence intensities and a thermal relative sensitivity of $S_r = 1.31\%$ K^{-1} and temperature uncertainties in the range of ±1 K. In one of the presented materials, we were able to show that upconversion with 980 nm excitation also allows to perform efficient physiological luminescence thermometry between 20 and 60 °C in water upon usage of the $^2H_{11/2}$, $^4S_{3/2} \rightarrow {}^4I_{13/2}$ transitions of Er^{3+} located in BW-I. This thermometric measure shows a relative thermal sensitivity of $S_r = 0.70\%$ K^{-1} and even allows to detect temperatures with an uncertainty below ±1 K. Unlike the conventionally used green emission of Er^{3+}, the respective radiative transitions from the thermally coupled $^2H_{11/2}$ and $^4S_{3/2}$ to the higher energetic ground level $^4I_{13/2}$ located in BW-I perfectly matches the range of tissue transparency, which is highly beneficial for in vivo nanothermometry. Moreover, all materials were proven to be completely non-toxic to human fibroblastic cells even at high concentrations, which demonstrates their excellent potential as future nanothermometers for biological systems.

4. Experimental Section

General: $Ln(CF_3COO)_3$ (Ln = Gd, Er, Yb) precursors were prepared according to a previously reported protocol.[45] All other chemicals were commercially purchased and used without further purification.

Synthesis of Compound 1: For the synthesis of compound **1** (top down nanorattles), first hollow PMO particles needed to be prepared. This was done in two steps. SiO_2 nanoparticle cores were grown and then a PMO shell was grown around them. In a later step, the inner SiO_2 core was etched, which yielded hollow PMO particles.

The SiO_2 nanoparticle cores were prepared in the following way.[46] 74 mL ethanol, 10 mL distilled water, and 3.14 mL 36–38% ammonia solution was mixed and magnetically stirred in a flask placed in a water bath set at 30 °C. Next, 6 mL tetraethyl orthosilicate (TEOS) was quickly added under continuous stirring and the reaction was stopped after 1 h. The particles were kept in solution without further purification.

Core-shell SiO_2@PMO nanoparticles were prepared by mixing 1.2 g cetyltrimethylammonium bromide (CTAB), 20 mL ethanol, 110 mL distilled water, and 3 mL 36–38% ammonia solution in a flask.[46,47] The mixture was stirred at 30 °C until CTAB was completely dissolved. In a following step, the solution of SiO_2 core particles was added and left to stir for 30 min. Next, 3 mL BTEB was added dropwise and the reaction was carried out for 6 h. The product was collected by centrifugation (3000 RPM) and washed several times with water and ethanol before drying at 80 °C in air.

Hollow PMO particles were obtained by etching the SiO_2 core. This was done by mixing 0.1 g of the core-shell SiO_2@PMO nanoparticles in 20 mL distilled water with 0.636 g Na_2CO_3 in a flask. The mixture was heated to 80 °C and left to stir for 1 h. Afterward, the particles were centrifuged and washed several times with distilled water and dried at 80 °C in air. The final step ensured that the material was porous. For that purpose, CTAB was removed from the pores. Three extractions were carried out. In each extraction 100 mL ethanol and 1 mL concentrated HCl was used. The extractions were carried out at 80 °C for 6 h each.

Afterwards, the product was centrifuged and washed with both distilled water and ethanol for several times. It was dried in a vacuum oven at 120 °C overnight.

The final nanorattle compounds were obtained in the following procedure. In a typical procedure, 25 mg of the hollow PMOs prepared according to the previous description was placed in a three-necked flask. The flask was degassed for 1 h. Then, a solution of 1.16 g $Gd(CF_3COO)_3$, 0.3072 g $Yb(CF_3COO)_3$, 0.03036 g $Er(CF_3COO)_3$, and 1.02 g CF_3COONa dissolved in 2.5 mL distilled water was injected into the flask kept under vacuum.[48] The suspension was stirred at room temperature for additional 5 h under vacuum and left to stir overnight under ambient atmosphere afterward. It was then centrifuged at 2000 RPM, further dried at 80 °C in air and subsequently heat treated at 300 °C for 6 h under air atmosphere. The amount of β-$NaGdF_4$:Er^{3+}, Yb^{3+} loading could be controlled by the concentration of the injected solution as well as the reaction time.

Synthesis of Compound 2: For the synthesis of compound **2** (bottom up nanorattles), 5 nm average-sized β-$NaGdF_4$:Er^{3+}, Yb^{3+} nanocrystals were synthesized first, employing a co-precipitation synthesis route.

In a typical synthesis 0.1488 g $GdCl_3 \times 6$ H_2O, 0.0348 g $YbCl_3 \times 6$ H_2O, and 0.00382 g $ErCl_3 \times 6$ H_2O were placed in a three-necked flask. Then, 4 mL oleic acid and 6 mL 1-octadecene were added. The mixture was heated to 120 °C under vacuum for 1 h and cooled down to room temperature. Next, 0.17 g CF_3COONa was added and after sealing of the flask, the temperature was raised to 100 °C under vacuum to remove all water. After this step, the temperature was slowly raised to 300 °C under N_2 atmosphere and maintained there for 40 min. After cooling down back to room temperature, the particles were precipitated with ethanol, collected via centrifugation, and washed three times with cyclohexane and ethanol. Finally, they were redispersed in cyclohexane for storage.

Synthesis of nanorattles was carried out in three steps.[49] In the first step, 0.5 mL Igepal CO-520 was dissolved in 9 mL cyclohexane and stirred for a few minutes. Around 10 mg of the β-$NaGdF_4$:Er^{3+}, Yb^{3+}-cyclohexane dispersion was added to the mixture drop wise and stirred at room temperature for 3 h. Next, 0.75 mL 30% ammonia solution was added dropwise and the mixture stirred for additional 30 min. Then, 75 µL of TEOS was added and stirred for around 6 h. In a final step, a mixture of 160 µL BTEB and 80 µL APTES was added and stirred at room temperature overnight. The particles were precipitated the next day by addition of methanol, collected via centrifugation, and washed three times with cyclohexane and ethanol before redispersion in distilled water.

In order to etch out the SiO_2 layer and form voids in the core-shell structures, 0.055 g of the as-prepared particles were dissolved in 2.5 mL distilled water (dispersed using an ultrasound bath). 0.1 g of PVP was dissolved in 5 mL of distilled water in a flask. The core-shell-shell solution was added to the PVP solution and the resulting solution stirred at room temperature for 30 min. Subsequently, the mixture was heated to 98 °C and etched for 6 h. The product was washed three times with water and ethanol and finally dispersed in water.

Synthesis of Compound 3: For the synthesis of compound **3**, mesoporous silica nanoparticles (mSiO₂) were prepared in advance. In a typical procedure, 0.2 g CTAB, 25 mL distilled water, 5 mL ethanol, and 50 µL TEA were mixed and stirred at 60 °C for 30 min.[50] Next, 2 mL TEOS was added into the solution leaving it to stir for 2 h. A colorless solid precipitated from the solution, which was collected by centrifugation after the suspension had cooled down to room temperature. The mSiO₂ was next dried at 80 °C in air and the particles were further calcined at 550 °C under air atmosphere for 5 h to remove the organic additives.

In the second step of the synthesis, in an attempt to grow nanoparticles inside the pores of mSiO₂, the following steps were carried out. 0.044 g of the as prepared mSiO₂ was placed in a flask. Next, 0.59 g $Gd(CF_3COO)_3$, 0.1536 g $Yb(CF_3COO)_3$, 0.01518 g $Er(CF_3COO)_3$, and 0.51 g CF_3COONa were added to the flask. 5 mL of distilled water was added and the flask was closed and heated at 40 °C under stirring for 24 h. The suspension was centrifuged at 2000 RPM afterwards and left to dry in air at 80 °C. It was finally heat treated at 500 °C under air atmosphere.

Synthesis of Compound **4**: For the synthesis of compound **4**, the DPA-PMO was prepared first. This was done in a two-step synthesis of first the *N,N*-bis(triethoxysilyl)-2,6-pyridine dicarboxamide precursor followed by the subsequent desired PMO material. The *N,N*-bis(trimethoxysilylproply)-2,6-pyridine dicarboxamide (DPA-Si) was synthesized according to a previously reported protocol.[29] For the synthesis of DPA-PMO, 0.3 g of CTAB and 0.084 g NaOH were dissolved in 144 mL distilled water. The solution was stirred at 80 °C for 30 min until the surfactant was fully dissolved. Next, 0.1645 g of the pre-synthesized DPA-Si (viscous liquid) and TEOS (1.325 g) in 1 mL ethanol was added dropwise under stirring. A colorless precipitate formed immediately, and the resulting suspension was additionally stirred at 80 °C for 2 h. The suspension was centrifuged and the powder washed two times with water and once with ethanol. In order to remove the CTAB template, solvent extraction was performed three times. For 0.5 g of product, 100 mL of ethanol and 0.2 mL of 37% HCl were used (65 °C for 6 h). The solvent extraction was repeated two times to ensure full removal of the template.

In a next step, 0.044 g of the as-prepared DPA-PMO was placed in a flask. 0.59 g Gd(CF$_3$COO)$_3$, 0.1536 g Yb(CF$_3$COO)$_3$, 0.01518 g Er(CF$_3$COO)$_3$, and 0.51 g CF$_3$COONa and 5 mL of distilled water were added to the flask, which was then closed and heated to 40 °C under continuous stirring for 24 h. The suspension was centrifuged the next day at 2000 RPM and left to dry at 80 °C in air. The sample was finally heat treated at 300 °C under air atmosphere.

Tests and Characterization: Cell Cultivation: Fibroblastic cells of NHDF (Normal Human Dermal Fibroblasts) culture were cultured in DMEM (Cat. No. D5546) supplemented with 10% FBS, 2 mM glutamine, and 100 µg mL^{-1} penicillin/streptomycin. The media were replaced every three days, and the cells were maintained in a humidified incubator at 5% CO$_2$ and 37 °C (Innova CO-170, New Brunswick Scientific).

Tests and Characterization: Cell Viability: NHDF cells were seeded into 96-well cell culture plates at a cell density of 10×10^4 per well and incubated (Innova CO-170, New Brunswick Scientific) at 37 °C under 5% CO$_2$. After 24 h cultivation, PMO particles from 0.001 till 1 mg per well were placed into the plate in the culture medium and incubated overnight. Subsequently, cells were incubated for 4 h, together with 10 µL of fluorescence dye was added to each well (AlamarBlue, Sigma-Aldrich). In the last step fluorescent (540/610 nm) intensity was measured by a spectrophotometer (Synergy H1Multi-Mode Reader).

Tests and Characterization: Fluorescence Microscopy: Viable cells were visualized with a Nikon TI (Nikon, Japan) fluorescence microscope with a following objective 10× and appropriate filters. After one day of incubation with PMO particles, cell layers were stained with calcein AM. Cells were incubated with a medium containing 0.1 mM of the reagent at room temperature for 10 min.

Tests and Characterization: Luminescence Spectroscopy and Thermometry: Luminescence spectra were measured on an Edinburgh FLS920 spectrofluorometer equipped with a Hamamatsu R928P photomultiplier tube used to detect the emission signals in the near UV to visible range and a Hamamatsu R5509-72 NIR photomultiplier tube (PMT, Hamamatsu, Shizuoka, Japan) that was cooled with liquid N$_2$ to detect the NIR emission. All emission spectra were acquired by excitation with a continuous wave (CW) power-tunable (power limit: $P_{max} = 2$ W, Livingston, UK) laser operating at $\lambda_{ex} = 980$ nm. Temperature-dependent emission spectra above room temperature of the powders were measured in a Linkam (Surrey, UK) THMS600 Microscope Stage (±0.1 °C temperature stability) that could be placed in the spectrometer. Aqueous suspensions of the particles were measured using a QPOD 2e (Quantum Northwest, USA), which was placed in the spectrometer. Stirring at 800 RPM was employed during the measurements. Low temperature measurements were performed using an ARS (ARS Cryo, USA) closed cycle cryostat coupled with an Edinburgh Instruments FLSP920 UV–vis–NIR spectrometer setup. Here, a Hamamatsu R928P photomultiplier tube (PMT, Hamamatsu, Shizuoka, Japan) was used to detect the emission signals. The emission spectra were acquired by excitation with CW (power limit: $P_{max} = 800$ mW, Livingston, UK) laser operating at $\lambda_{ex} = 980$ nm. All emission spectra in the manuscript have been corrected for detector response and grafting efficiency. All the temperature-dependent data were processed employing the TeSen software: http://www.tesen.ugent.be.[51]

Tests and Characterization: TEM, Powder X-Ray Diffraction, N$_2$ Sorption: TEM images were taken on a JEOL JEM-2200FS TEM operated at 200 kV and equipped with C$_s$ corrector. The samples were prepared by dipping a 300-mesh holey carbon copper grid into the purified nanoparticle suspensions. Scanning TEM (STEM) images were taken with high-angle annular dark field (HAADF) detector. The composition of the sample was determined via EDX spectroscopy in HAADF-STEM mode. Powder XRD patterns were recorded by a Thermo Scientific ARL X'TRA diffractometer equipped with a Cu Ka (l = 1.5405 Å) source, a goniometer, and a Peltier cooled Si (Li) solid-state detector. Nitrogen adsorption–desorption isotherms were measured by using a Micromeritics TriStar 3000 analyzer at −196 °C. The samples were vacuum dried for 24 h at 120 °C before the measurements. Surface areas were calculated using the Brunauer–Emmett–Teller (BET) method.

Supporting Information

Supporting Information is available from the Wiley Online Library or from the author.

Conflict of Interest

The authors declare no conflict of interest.

[1] M. Dramicanin, *Luminescence Thermometry, Methods, Materials and Applications*, 1st ed., Woodhead Publishing, Cambridge **2018**.

[2] C. D. S. Brites, S. Balabhadra, L. D. Carlos, *Adv. Opt. Mater.* **2018**, 7, 1801239.

[3] D. Jaque, F. Vetrone, *Nanoscale* **2012**, 4, 4301.

[4] L. D. Carlos, F. Palacio, *Thermometry at the Nanoscale: Techniques and Selected Applications*, Royal Society of Chemistry, Oxfordshire **2016**.

[5] J. Rocha, C. D. S. Brites, L. D. Carlos, *Chem. - Eur. J.* **2016**, 22, 14782.

[6] Y. Zhou, B. Yin, F. Lei, *Chem. Commun.* **2014**, 50, 15235.

[7] Z. Wang, D. Ananias, A. Carne-Sanchez, C. D. S. Brites, I. Imaz, D. Maspoch, J. Rocha, L. D. Carlos, *Adv. Funct. Mater.* **2015**, 25, 2824.

[8] D. Wawrzynczyk, A. Bednarkiewicz, M. Nyk, W. Strek, M. Samoc, *Nanoscale* **2012**, 4, 6959.

[9] C. D. S. Brites, P. P. Lima, N. J. O. Silva, A. Millan, V. S. Amaral, F. Palacio, L. D. Carlos, *Nanoscale* **2012**, *4*, 4799.

[10] J. Feng, L. Xiong, S. Wang, S. Li, Y. Li, G. Yang, *Adv. Funct. Mater.* **2013**, *23*, 340.

[11] F. Vetrone, R. Naccache, A. Zamarron, A. J. de la Fuente, F. Sanz-Rodriguez, L. M. Maestro, E. M. Rodriguez, D. Jaque, J. G. Sole, J. A. Copobianco, *ACS Nano* **2010**, *4*, 3254.

[12] X. Liu, S. Akerboom, M. de Jong, I. Mutikainen, S. Tanase, A. Meijerink, E. Bouwmam, *Inorg. Chem.* **2015**, *54*, 11323.

[13] Y. Gao, F. Huang, H. Lin, J. Zhou, J. Xu, *Adv. Funct. Mater.* **2016**, *18*, 3139.

[14] Z. Antic, M. D. Dramicanin, K. Prashanthi, D. Jovanovic, S. Kuzman, T. Thundat, *Adv. Mater.* **2016**, *28*, 7745.

[15] A. Cadiau, C. D. S. Brites, P. M. F. J. Costa, R. A. S. Ferreira, J. Rocha, L. D. Carlos, *ACS Nano* **2013**, *7*, 7213..

[16] A. M. Kaczmarek, *J. Mater. Chem. C* **2018**, *6*, 5916.

[17] A. M. Kaczmarek, M. K. Kaczmarek, R. Van Deun, *Nanoscale* **2019**, *11*, 833.

[18] T. Xia, Y. Cui, Y. Yanga, G. A. Qian, *J. Mater. Chem. C* **2017**, *5*, 5044.

[19] M. Suta, Z. Antic, V. Dordevic, S. Kuzman, M. D. Dramicanin, A. Meijerink, *Nanomaterials* **2020**, *10*, 543.

[20] A. M. Kaczmarek, Y.-Y. Liu, M. K. Kaczmarek, H. Liu, F. Artizzu, L. D. Carlos, P. Van der Voort, *Angew. Chem., Int. Ed.* **2020**, *59*, 1932.

[21] J.-C. G. Bünzli, C. Piguet, *Chem. Soc. Rev.* **2005**, *34*, 1048.

[22] J.-C. G. Bünzli, *Acc. Chem. Res.* **2006**, *39*, 53.

[23] U. Kostiv, M. Slouf, H. Mackova, A. Zhigunov, H. Engstova, K. Smolkova, P. Jezek, D. Horak, *Beilstein J. Nanotechnol.* **2015**, *6*, 2290.

[24] M. Zhou, X. Ge, D.-M. Ke, H. Tang, J.-Z. Zhang, M. Calvaresi, B. Gao, L. Sun, Q. Su, H. Wang, *Front. Chem.* **2019**, *7*, 218.

[25] J. G. Croissant, Y. Fatieiev, A. Almalik, N. M. Khashab, *Adv. Healthcare Mater.* **2017**, *7*, 1700831.

[26] J. G. Croissant, X. Cattoen, M. W. C. Man, J.-O. Durand, N. M. Khashab, *Nanoscale* **2015**, *7*, 20318.

[27] S. He, J. Song, J. Qu, Z. Cheng, *Chem. Soc. Rev.* **2018**, *47*, 4258.

[28] A. M. Kaczmarek, Y. Maegawa, A. Abalymov, A. G. Skirtach, S. Inagaki, P. Van der Voort, *ACS Appl. Mater. Interfaces* **2020**, *12*, 13540.

[29] A. M. Kaczmarek, R. Van Deun, P. Van der Voort, *J. Mater. Chem. C* **2019**, *7*, 4222.

[30] X. Fang, C. Chen, Z. Liu, P. Liu, N. Zheng, *Nanoscale* **2011**, *3*, 1632.

[31] D. Esquivel, A. M. Kaczmarek, C. Jimenez-Sanchidrian, R. Van Deun, F. J. Romero-Salguero, P. Van der Voort, *J. Mater. Chem. C* **2015**, *3*, 2909.

[32] Y. Su, L.-N. Hao, K. Liu, J. Zhang, L. Dong, Y. Xu, Y. Lu, H.-S. Qian, *RSC Adv.* **2018**, *8*, 12944.

[33] J. Liu, A. M. Kaczmarek, J. Billet, I. Van Driessche, R. Van Deun, *Dalton Trans.* **2016**, *45*, 12094.

[34] J. Liu, R. Van Deun, A. M. Kaczmarek, *Nanomaterials* **2019**, *9*, 646.

[35] F. T. Rabouw, P. T. Prins, P. Villanueva-Delgado, M. Castelijns, R. G. Geitenbeek, A. Meijerink, *ACS Nano* **2018**, *12*, 4812.

[36] A. M. Kaczmarek, J. Liu, B. Laforce, L. Vincze, K. Van Hecke, R. Van Deun, *Dalton Trans.* **2017**, *46*, 5781.

[37] A. M. Kaczmarek, Y.-Y. Liu, C. Wang, B. Laforce, L. Vincze, P. Van der Voort, R. Van Deun, *Dalton Trans.* **2017**, *46*, 12717.

[38] W. T. Carnall, P. R. Fields, K. Rajnak, *J. Chem. Phys.* **1968**, *49*, 4424.

[39] A. Ciric, J. Aleksic, T. Barudzija, Z. Antic, V. DOrdevic, M. Medic, J. Perisa, I. Zekovic, M. Mitric, M. D. Dramicanin, *Nanomaterials* **2020**, *10*, 627.

[40] A. G. Skirtach, A. Munoz Javier, O. Kreft, K. Kohler, A. Piera Alberola, H. Mohwald, W. J. Parak, G. B. Sukhorukov, *Angew. Chem., Int. Ed.* **2006**, *45*, 4612.

[41] ISO 10993-5:2009, Biological evaluation of medical devices—Part 5: Tests for in vitro cytotoxicity, Canadian Standards Association **2007**, pp. 1–11.

[42] Y. Shen, J. Lifante, N. Fernandez, D. Jaque, E. Ximendes, *ACS Nano* **2020**, *14*, 4122.

[43] S. Balabhadra, M. L. Debasu, C. D. S. Brites, R. A. S. Ferreira, L. D. Carlos, *J. Phys. Chem. C* **2017**, *121*, 13962.

[44] Q. Zhan, J. Qian, H. Liang, G. Somesfalean, D. Wang, S. He, Z. Zhang, S. Andersson-Engels, *ACS Nano* **2011**, *5*, 3744.

[45] J. Liu, H. Rijckaert, M. Zeng, K. Haustraete, B. Laforce, L. Vincze, I. Van Driessche, A. M. Kaczmarek, R. Van Deun, *Adv. Funct. Mater.* **2018**, *28*, 1707365.

[46] X. Qian, W. Wang, W. Kong, Y. Chen, *RSC Adv.* **2014**, *4*, 17950.

[47] S. Haffer, M. Tiemann, M. Fröba, *Chem. - Eur. J.* **2010**, *16*, 10447.

[48] S. Lu, D. Tu, X. Li, R. Li, X. Chen, *Nano Res.* **2016**, *9*, 187.

[49] S. Lu, D. Tu, P. Hu, J. Xu, R. Li, M. Wang, Z. Chen, M. Huang, X. Chen, *Angew. Chem., Int. Ed.* **2015**, *54*, 7915.

[50] Y. Li, Y. Zhou, T. Gu, G. Wang, Z. Ren, W. Weng, X. Li, G. Han, C. Mao, *Part. Part. Syst. Charact.* **2016**, *33*, 896.

[51] A. M. Kaczmarek, R. Van Deun, M. K. Kaczmarek, *Sens. Actuators, B* **2018**, *273*, 696.